JOURNAL OF MATERIALS SCIENCE 26 (1991) 940–950

The presence and consequences of precipitate-free zones in an aluminium–copper–lithium alloy

T. S. SRIVATSAN*
Department of Mechanical Engineering, The University of Akron, Akron, Ohio 44325, USA
E. J. LAVERNIA‡
Division of Materials, Department of Mechanical Engineering, University of California, Irvine, California 92717, USA

The addition of lithium to aluminium alloys has the potential for providing a class of high-strength alloys with exceptional properties suitable for aerospace applications. Potential candidates are precipitation hardenable and belong to the Al–Li–Cu family. The intrinsic microstructural features have a pronounced influence on the mechanical response of these alloys. In this work, the mechanisms responsible for the formation of precipitate-free zones along grain boundaries in precipitation-strengthened lithium-containing aluminium alloys were examined. The influence of grain morphology and the nature and type of precipitate coverage at the grain boundary in controlling the formation of these zones was analysed. The presence and influence of these zones along the grain boundaries on mechanical properties was studied for an Al–4.5Cu–1.21Li alloy. It was found that while strength is comparable with existing high-strength alloys, the ductility decreases due to the presence of precipitate-free zones. The degradation in ductility is attributed to the particular mode of plastic deformation of this alloy, and to the restriction of plastic deformation in narrow planar zones along the grain boundaries. Fracture occurs when a critical local strain is reached in these zones. The overall consequences of precipitate-free zones along grain boundaries on mechanical properties are discussed in the light of competing effects involving the nature of matrix-strengthening precipitates, grain-boundary particles and deformation characteristics.

1. Introduction

During the isothermal ageing sequence, precipitation-hardenable aluminium alloys exhibit a condition in which the interior of the grains is highly hardened while the grain boundary and its surrounding environment is very soft and weak. Since the pioneering work by Geisler [1] on the formation of weak denuded zones in precipitation-hardenable alloys, several intensive investigations have been conducted to understand the mechanisms responsible for the formation of these zones in high-strength aluminium alloys (e.g. [2–8]). The zones adjacent to grain boundaries are relatively free or totally devoid of precipitates. Geisler claimed that these zones were anodic paths for stress corrosion [1]. This was attributed to a localized depletion of solute atoms caused by preferential precipitation at grain boundaries [2]. Subsequent studies by Thomas and Nutting [3], Taylor [4] and Embury and Nicholson [5] revealed that the zones adjacent to grain boundaries were due to an absence of a critical vacancy concentration required for precipitate nucleation in the vicinity of grain boundaries. According to Thomas and Nutting [3], vacancy depletion was a key factor in controlling the width of the denuded zone. This observation led Kelly and Nicholson [6] to define these zones as "precipitate-free". Thus, adjacent to grain boundaries there exists two kinds of zones, or denuded regions that are totally devoid of precipitates: (a) those caused by solute depletion, and (b) those arising from vacancy depletion. The "denuded" regions were referred to as precipitate-free zones (PFZs).

In precipitation-hardenable, high-strength aluminium alloys, nucleation and growth of Guinier–Preston (GP) zones at temperatures below the GP zone solvus, and the transformation of those GP zones that acquire a critical size to precipitates upon ageing at temperatures above the GP zone solvus, resulted in the formation of PFZs [7, 8]. Subsequent studies have considered the effects of: (a) slow quench and quench interruption treatments [9], and (b) the effects of time and temperature of ageing [10] on PFZ formation. The width of the PFZ was observed to increase with time of ageing only below the GP zone solvus temperature [10].

* *Previous address*: Materials Modification Inc., Falls Church, Virginia 22044, USA
‡ *Previous address*: Massachusetts Institute of Technology, Cambridge, Massachusetts 02139, USA.

0022–2461/91 $03.00 + .12

The objective of this work was to examine the influence of PFZs on the monotonic ductility, deformation and fracture behaviour of an ingot metallurgy (IM) aluminium–copper–lithium alloy, and to compare the results with those of equivalent alloys processed using powder metallurgy (PM), rapid solidification (RS) techniques. Interest in the aluminium–lithium system is due to its well-documented precipitation characteristics and its emergence as a commercial alloy for aerospace applications. Before describing the consequences of PFZs on properties, the influence of microstructure and the intrinsic micromechanisms responsible for the formation of these zones in aluminium alloys are discussed.

2. Formation of PFZs

Grain and subgrain boundaries lower the surface and strain energies of precipitates. Consequently, it is logical to assume that they would be preferred sites for the nucleation of partially coherent and incoherent phases. However, it is logical to assume that they should have a negligible effect on the formation of coherent clusters or GP zones [11]. When the precipitates form at and along the grain boundaries from the same solute additions as the matrix precipitates, a PFZ results. The orientation relationship between grains was observed to have a marked influence on adjacent grains [12]. In this study, Cornish and Day found grain-boundary precipitate distribution to be related to grain-boundary misorientation. At low-angle grain boundaries, that is, along boundaries corresponding to angular misorientations of $< 10 \pm 2°$, the grain-boundary precipitates were more finely dispersed than along a great majority of high-angle grain boundaries. This process also resulted in variable width of the PFZs being formed on low-angle boundaries. On the high-angle grain boundaries, the particles were fewer and further apart, and a uniform PFZ resulted. Unwin and Nicholson [13] showed that the grain-boundary precipitate nucleation could occur in two stages, with the nucleation and growth of the precipitates being strongly influenced by the type of grain boundary However, in some aluminium alloys (for example the Al–Zn–Mg) [14, 15] the PFZ results due to a vacancy-loss mechanism such that a PFZ without any grain-boundary particles is possible.

In precipitation-hardenable aluminium–lithium alloys the PFZs have been observed adjacent to high-angle grain boundaries (Fig. 1), low-angle grain boundaries and at grain-boundary triple junctions (Fig. 2). Explanations for the formation of these zones have been based upon a vacancy-depletion or a solute-depletion mechanism [16–18]. In the vacancy-depletion mechanism, a vacancy-concentration profile develops in the immediate vicinity of grain boundaries in the case of solution heat-treated and quenched alloy. Furthermore, it is assumed that in the formation of a vacancy-depleted PFZ the solute concentration is uniform throughout the grains, and no solute has segregated to the grain boundaries during the quench. An excess vacancy profile develops in the vicinity of grain boundaries for some period after quenching from the quench temperature to the ageing temperature. This occurs because the grain boundaries are sinks or conductors for vacancies, and the annihilation of vacancies at grain boundaries or the motion of vacancies along grain boundaries to surfaces is controlled by the diffusion of vacancies within the grain [19, 20]. The shape of the vacancy profile depends on the quenching temperature, because the equilibrium concentration of vacancies increases both with temperature and quenching rate. A schematic illustration of an excess vacancy profile is shown in Fig. 3. While slower quenching rates provide for diffusion over larger distances resulting in a decreased slope in the profile, rapid quenching from an elevated temperature will result in steeper concentration gradients.

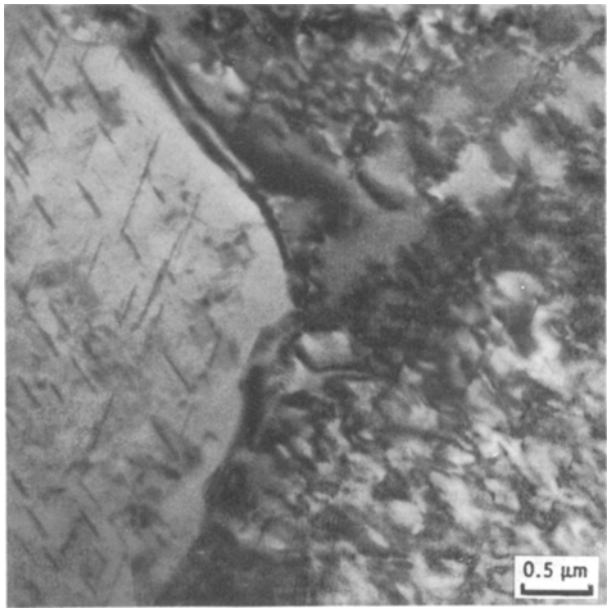

Figure 1 Bright-field transmission electron micrograph showing PFZ along a high-angle grain boundary in an IM Al–4.5Cu–1.21Li alloy.

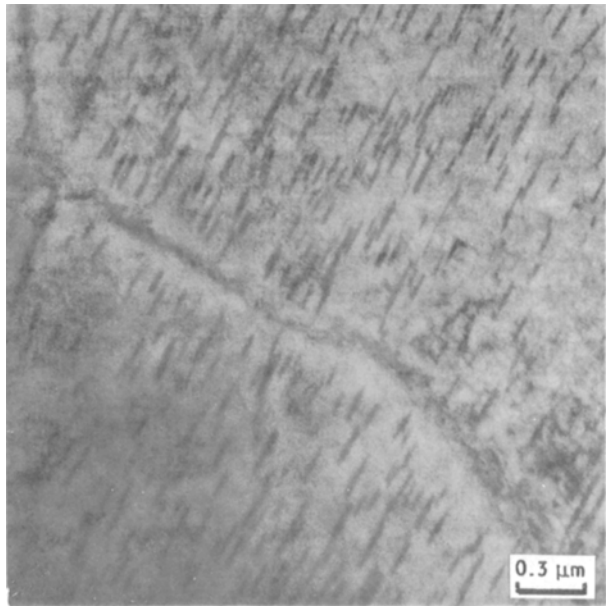

Figure 2 Bright-field transmission electron micrograph showing PFZ at grain-boundary triple junction in an IM Al–4.5Cu–1.21Li alloy.

At temperatures above the critical temperature for homogeneous nucleation, an excess critical vacancy concentration is required for nucleation of the precipitating phase. Near the grain boundaries, the vacancy concentration is less than a critical value and hence no precipitates form. Consequently, a PFZ results. Fig. 3 defines the vacancy-depleted PFZ for a sample quenched from a higher quenching temperature, and the vacancy-depleted PFZ for the sample quenched from a medium and low quenching temperature.

In the mechanism of solute depletion, solute is lost from the immediate vicinity of a grain boundary during the quench due to:

(a) heterogeneous nucleation of precipitates on the grain boundary during cooling to the ageing temperature, and

(b) preferential segregation of solute atoms to grain boundaries after solution heat treatment and quenching.

In either case, a solute concentration profile develops near the grain boundary. The profile depends on both the structure and misorientation of the grain boundary, on account of the influence of these parameters on the nucleation of grain-boundary precipitates [21]. At a certain temperature there is a critical solute concentration (C_s) that is required for the homogeneous nucleation of the precipitate phase to occur within the region of solute depletion. The critical solute concentrations, C_s, for various temperatures are shown as horizontal lines in Fig. 4. Intersection of the horizontal lines in Fig. 4 with the solute-concentration profile gives the width of the solute-depleted PFZ. The width of the PFZ that is shown schematically in Fig. 5 and formed due to solute depletion, is governed by several parameters which include: (i) alloy composition, (ii) homogenization, (iii) ageing temperature, (iv) quenching rate, (v) heating rate, and (vi) holding time and temperature.

When lithium-containing aluminium alloys containing sufficient solute are quenched from a single-phase field and aged below the critical temperature for homogeneous nucleation, the supersaturated solid solution (SSSS) decomposes homogeneously to give metastable and equilibrium phases. The metastable precipitate phase is $\delta'(Al_3Li)$. The precipitate has an $L1_2$-type superlattice structure equivalent to a preferred positioning of lithium atoms on one of the four sublattices in a face-centred cubic structure (Fig. 6).

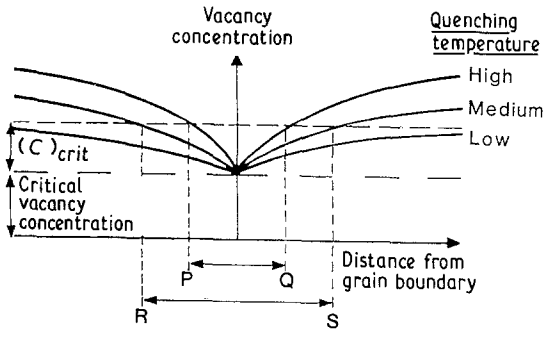

Figure 3 Schematic drawing showing the excess vacancy concentration profile [14, 16].

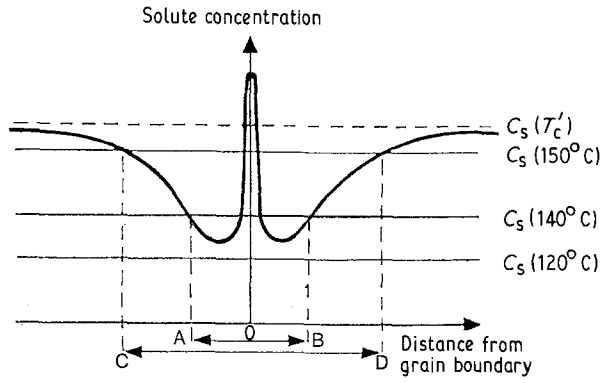

Figure 4 Schematic drawing showing the solute concentration profile and the solute-depleted PFZ in the vicinity of the grain boundary [16]. T_c the highest temperature for homogeneous nucleation with excess vacancies.

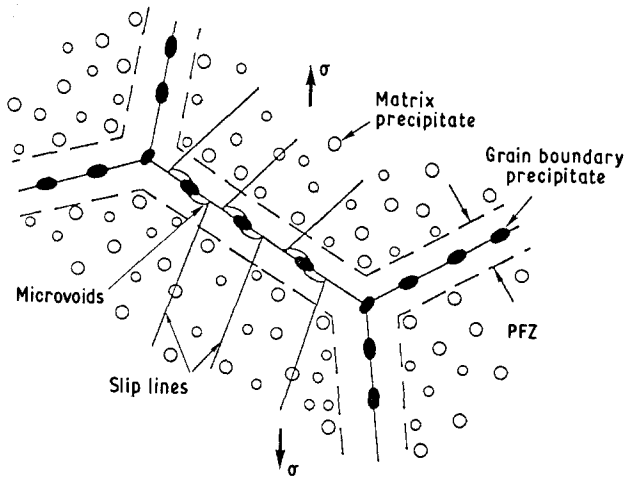

Figure 5 Schematic drawing showing the intrinsic microstructural features and PFZ along the grain boundary in an aluminium–lithium–copper alloy [15].

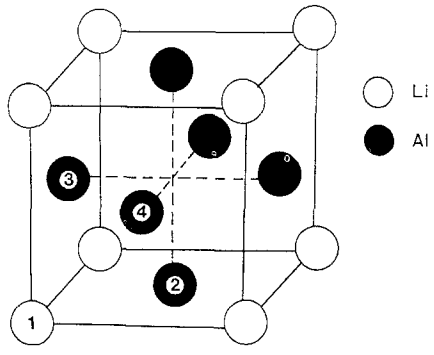

Figure 6 The $L1_2$ unit cell, the structure of Al_3Li. Precipitation δ' is effectively a clustering and ordering of lithium atoms within the f c c aluminium solid solution.

The δ' has a spherical shape possessing a cube/cube orientation with respect to the matrix [22–24]. These precipitates have a crystallographic structure similar to that of the matrix and a small lattice misfit. During ageing at higher temperatures (artificial ageing) the precipitate particles coarsen. The coarsening rate with time follows the Ostwald ripening kinetics [25]. In addition to coarsening of the $\delta'(Al_3Li)$ precipitates in the matrix, preferential growth of the equilibrium δ(AlLi) precipitate occurs on the grain boundary. The

solute necessary for the continued growth of the equilibrium AlLi precipitate is provided by the dissolution of particles in the vicinity of grain boundaries [26]. Consequently, a PFZ develops. The PFZs due to δ′ dissolution have been shown to grow with ageing time [27, 28]. In both these studies the experimental data were fitted to a growth law where the PFZ width was found to be proportional to t^n, with t being the ageing time and n a constant.

In a recent study, Jha *et al.* [26] observed the grain morphology to have an influence on the width of the PFZ in aluminium–lithium alloys. Growth of the PFZ was found to be diffusion controlled and parabolic with time. A considerable amount of scatter in the width of the PFZ was observed in an unrecrystallized zirconium-containing Al–2.8% Li alloy than in a recrystallized Al–2.8% Li alloy containing manganese as the grain refiner. The researchers attributed the scatter or non-uniform PFZ width to:

(a) the highly non-uniform nature of grain boundaries, and

(b) the distribution of particles amongst the various grain boundaries in the zirconium-containing alloy.

Narrow or no PFZs were observed at the small-angle grain boundaries and twist boundaries of this alloy. While the high-angle grain boundaries are associated with higher energy, and consequently, are potential sites for the heterogeneous nucleation of equilibrium δ particles. The growth of the PFZ in the unrecrystallized zirconium-containing alloy was observed to be higher than that in the recrystallized alloy having similar lithium content. The growth of the PFZ was also observed to increase with lithium content in the alloy. This behaviour was rationalized as being due to a possible increase in the interdiffusion coefficient with alloy composition [26].

3. Materials and experimental procedure

3.1. Material

An alloy based on the Al–Li–Cu system was chosen for this study. The ingot alloy had a chemical composition (wt %) 4.5% Cu, 1.21% Li, 0.51% Mn, 0.20% Cd, 0.16% Fe, 0.08% Si and balance aluminium. The microstructure of the alloy was examined in detail and the intrinsic microstructural features correlated with mechanical, deformation and fracture behaviour. The results are compared with those obtained for rapidly solidified aluminium–copper–lithium alloys of near equivalent composition [29, 30].

3.2. Microscopy

In order to characterize the size and morphology of the grains, samples for optical microscopy were mounted, mechanically polished on 320, 400 and 600 grit silicon carbide paper using water as a lubricant and then with 1 and 0.3 μm alumina. The samples were etched by an anodizing technique or by using Kellers etchant to reveal the high-angle grain boundaries. The specimens were then examined in an optical microscope and photographed using polarized light.

Fine microstructural features were revealed by transmission electron microscopy. Samples 0.5 to 1 mm thick were sliced from the bulk material. Thin foils for TEM investigation were prepared from discs of 3 mm diameter, cut, ground and thinned using a twin-jet electropolishing device. The electrolyte used was a 1:2 solution mixture of nitric acid in methanol maintained at a temperature of 253 K (−20 °C) and at a potential difference of 15 V. The foils were examined in a scanning transmission electron microscope (STEM) operating at 100 kV.

4. Results and discussion

4.1. Microstructure

The microstructure of the conventionally processed ingot alloy has been described in detail elsewhere [31–34]. This material is partially recrystallized with the recrystallized grains as large as 1500 μm and flattened and elongated along the rolling direction. The iron and silicon contents in the alloy are impurity elements. During ingot solidification and subsequent processing, these impurities precipitate as insoluble coarse constituent particles. These particles have been identified by electron microprobe and Guinier-de-Wolff X-ray diffraction method as compounds of Al_7Cu_2Fe, $Al_{12}(FeMn)_3Si$, $Al_{20}Cu_2Mn_3$ and Al_2CuLi. The coarse constituent particles ranged in size from 1 to 10 μm in the longest dimension [35]. In addition to coarse constituent particles, a small volume fraction of smaller particles of the Al_6Mn type were also present. These particles ranged in size from 0.2 to 1 μm and are shown in Fig. 7.

Copper addition to the alloy results in the formation of the coherent metastable precipitate θ′(Al_2Cu), which is the principal strengthening phase in the peak-aged maximum strength condition (Fig. 8). Lithium combines with aluminium to form the ternary T_1(Al_2CuLi) phase which is partially coherent with the aluminium matrix. Remaining lithium not used up in the formation of the ternary phase, combines with aluminium to form the binary metastable δ′(Al_3Li)

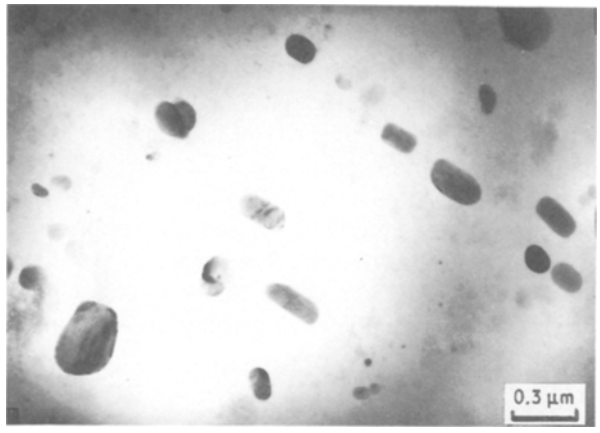

Figure 7 Bright-field transmission electron micrograph showing distribution of small constituent particles in the IM Al–4.5Cu–1.21Li alloy.

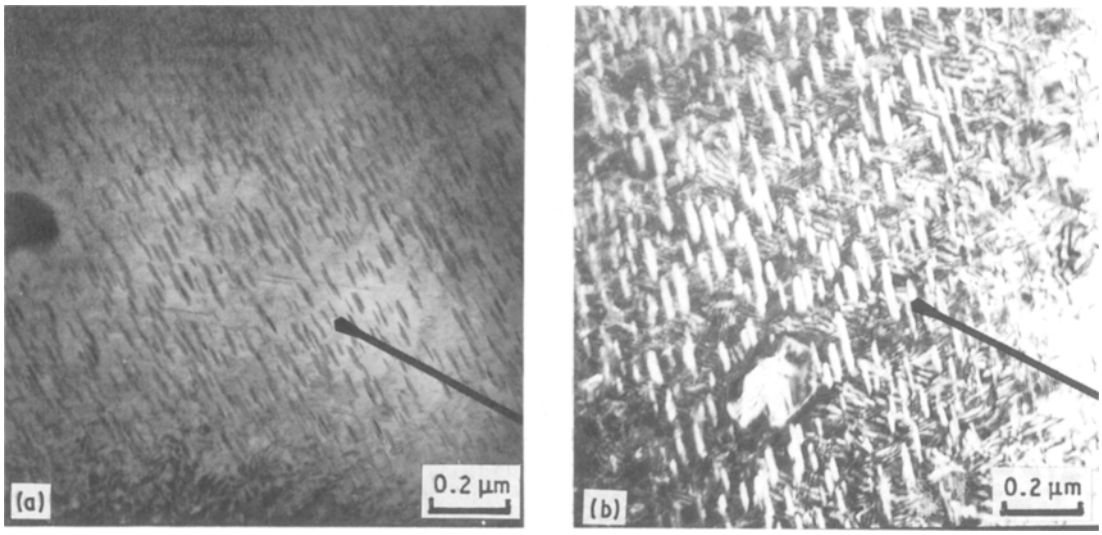

Figure 8 Bright-field transmission electron micrograph showing the principal strengthening phase θ′ in the IM Al–4.5Cu–1.21Li alloy: (a) bright-field, (b) dark-field.

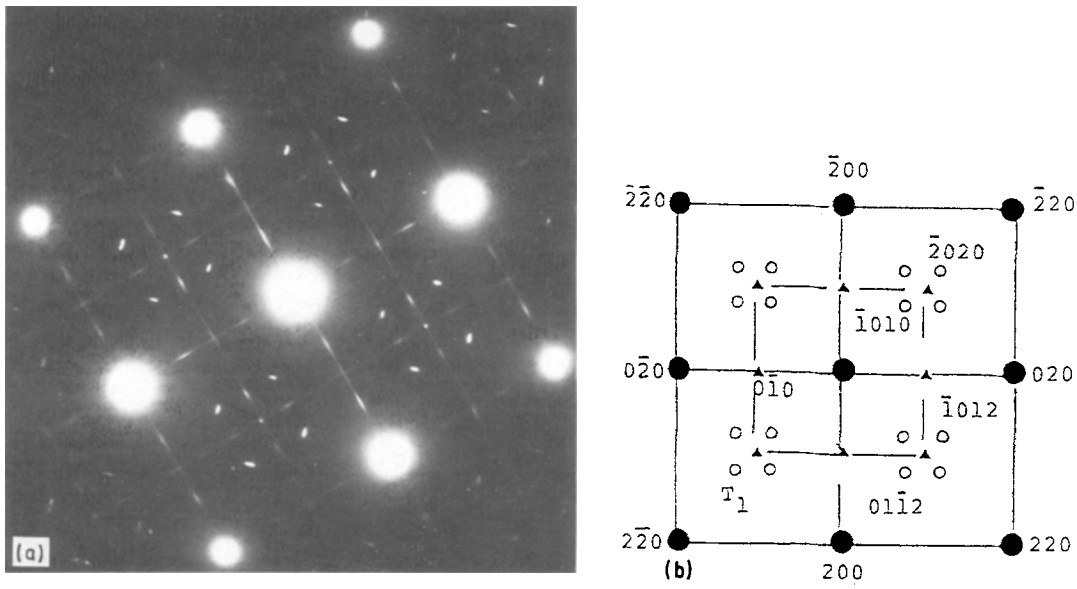

Figure 9 A typical (1 0 0) selected-area diffraction pattern for the Al–Li–Cu alloy. Superlattice spots caused by T_1 and δ reflections.

phase which is coherent with the fcc matrix. Cadmium plays the role of nucleating agent in the ingot alloy. It suppresses the precipitation of θ″ and increases the density of θ′, besides reducing the growth kinetics by segregating to the θ′/matrix interface [36, 37]. Manganese is the grain-refining element. It forms incoherent dispersoids, $Al_{20}Cu_2Mn_3$, which control the grain size, degree of recrystallization and the microscopic homogeneity of deformation.

Fig. 9 shows a typical (1 0 0) electron diffraction pattern of the ternary Al–Cu–Li alloy. The superlattice spots are due to δ′(Al_3Li) and the satellite spots due to the T_1 precipitates. The streaking parallel to the $[1\,0\,0]_{Al}$ directions is due to the θ′ phase. These precipitate particles have an orientation relationship

$$[1\,0\,0]_{matrix} \parallel [1\,0\,0]_{\theta'}$$

$$[2\,1\,1]_{matrix} \parallel [1\,1\,\bar{2}\,0]_{T_1}$$

In the peak-aged condition, the major strengthening precipitates in the ternary Al–Cu–Li ingot alloy are coherent and partially coherent with the aluminium matrix. Narrow PFZs, 0.05 μm wide were observed along the high-angle grain boundaries and at grain-boundary triple junctions in the ingot Al–4.5Cu–1.21Li alloy as is shown in Figs 1 and 2.

Kang and Grant [29, 30] studied the structure and properties of two powder–metallurgy processed X2020-type alloys (Alloy 68, Al–4.93Cu–1.19Cu–0.39Mn–0.11Cd; and Alloy 69, Al–4.40Cu–1.55Li–0.38Mn–0.15Cd) produced by inert-gas atomization using the ultrasonic gas-atomization process, followed by hot extrusion with an extrusion ratio of 20 to 1. The heat-treatment process on the extruded alloys is described in detail elsewhere [29] and will not be repeated here. The microstructures of the extruded and heat-treated PM alloys are shown in Fig. 10. In comparison with the microstructure of the ingot metallurgy Al–4.5Cu–1.21Li–0.51Mn alloy, the microstructure of the PM alloys consisted of very fine grains. The grain sizes determined for Alloy 68 and Alloy 69 were in the range 1 to 5 μm, with relatively

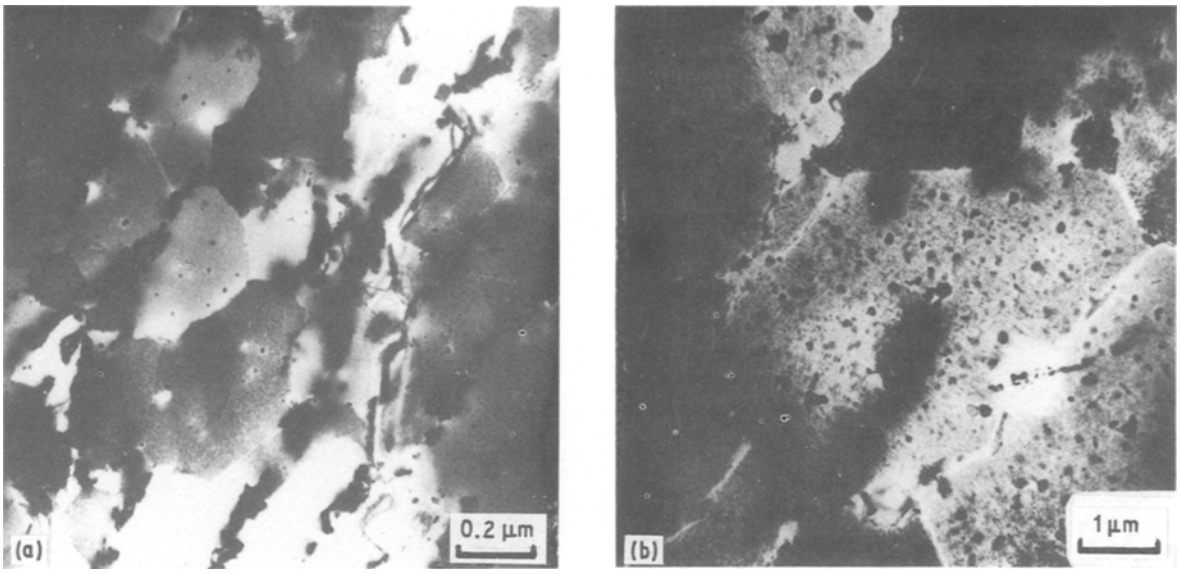

Figure 10 Bright-field transmission electron micrograph showing grain structure and oxide distribution in the RS PM alloys: (a) Alloy 68 (Al–4.93Cu–1.19Li)-T6, (b) Alloy 69 (Al–4.40Cu–1.55Li)-T7.

low aspect ratio, that is, the grains were elongated in the extrusion direction. Also evident from transmission electron microscopy was the presence of oxide phases decorating the prior particle boundaries as dark stringers. The oxide phases are formed during synthesis and consolidation of the rapidly solidified PM particulates. Their formation is a result of the extreme reactivity of both aluminium and lithium coupled with the large surface area associated with fine PM particulates. The presence of oxide phases in the form of continuous network or stringers is highly detrimental to the mechanical behaviour of consolidated PM materials by providing potential sites for premature crack initiation and preferred crack propagation. Consequently, complete inter-particle bonding is hindered and microporosity is promoted through gas desorption [38–47]. Alloy 69 was found to have less continuous oxide stringers than Alloy 68. The presence of relatively continuous oxide stringers in Alloy 68 was observed to have a detrimental effect on mechanical properties [29, 30].

Alloy 68 in the peak-aged (PA) (T6), maximum strength condition, was also observed to have a high volume fraction of the $\theta'(Al_2Cu)$ and $T_1(Al_2CuLi)$ phases dispersed throughout the grains, with PFZs along the grain boundaries [30]. The θ phase was observed only after solution heat treatment at high temperatures (798 K), and was not a major precipitate in this alloy. Also observed along the grain boundaries were the manganese-containing dispersoids ($Al_{20}Cu_2Mn_3$) of about 0.2 μm in size. The microstructure of Alloy 69 in the T7 condition was found to have very similar microstructure to those of the peak-aged (T6) Alloy 68 except for differences in the volume fraction of the major strengthening precipitates $\theta'(Al_2Cu)$ and T_1 [30]. In both Alloy 68 (Al–4.93Cu–1.19Li–0.39 Mn) and Alloy 69 (Al–4.4Cu–1.55Li–0.38Mn) the $\theta'(Al_2Cu)$ and $T_1(Al_2CuLi)$ precipitates dominated over other phases, implying their contribution to the observed strength and matrix deformation characteristics of these alloys. Kang and Grant [30] also alluded, through selected-area diffraction (SAD) analysis, to the presence of the $T_B(Al_{15}Cu_8Li_2)$ phase in Alloy 68-T6 and Alloy 69-T7. Formation of the T_B phase was rationalized as being due to the transformation of the θ' phase in the presence of lithium. However, they made no effort to ascertain the precise role of the T_B phase on the mechanical behaviour of the two rapidly solidified powder-metallurgy processed Al–Cu–Li alloys. The width of the PFZ was reported to range from 0.02 to 0.1 μm, with no consistent pattern among the two alloys (Fig. 11).

4.2. Mechanical behaviour

The monotonic properties of the ingot alloy at ambient temperature are listed in Table I along with the properties of 7075-T651, 2090-T841, 8090-T851 and 2024-T851 for comparison. Duplicate samples of the 2020 alloy were tested and no significant variation between the pairs of samples was observed. While the yield strength and tensile strength of the ingot Al–4.5Cu–1.21Li alloy is comparable with the other high-strength commercial aluminium alloys, the tensile ductility is inferior when compared with the existing commercial aluminium alloys.

The deformation behaviour of the ingot alloy was examined and found to be planar with the tendency toward strain localization. Fig. 12 shows planar deformation in the peak-aged tensile samples.

The ambient temperature tensile properties of the IM alloy are compared with the RS PM alloys in Table II. In general, the RS PM alloys exhibit higher strength levels when compared to the ingot alloy. The higher or improved strength of the RS PM alloys is rationalized by the effective role of oxides in inhibiting recrystallization and maintaining a refined microstructure. In addition, the fine dispersion of oxide phases will most likely provide a limited amount of dispersion strengthening. Also, the RS PM Al–Cu–Li alloys show marginal improvement in tensile elonga-

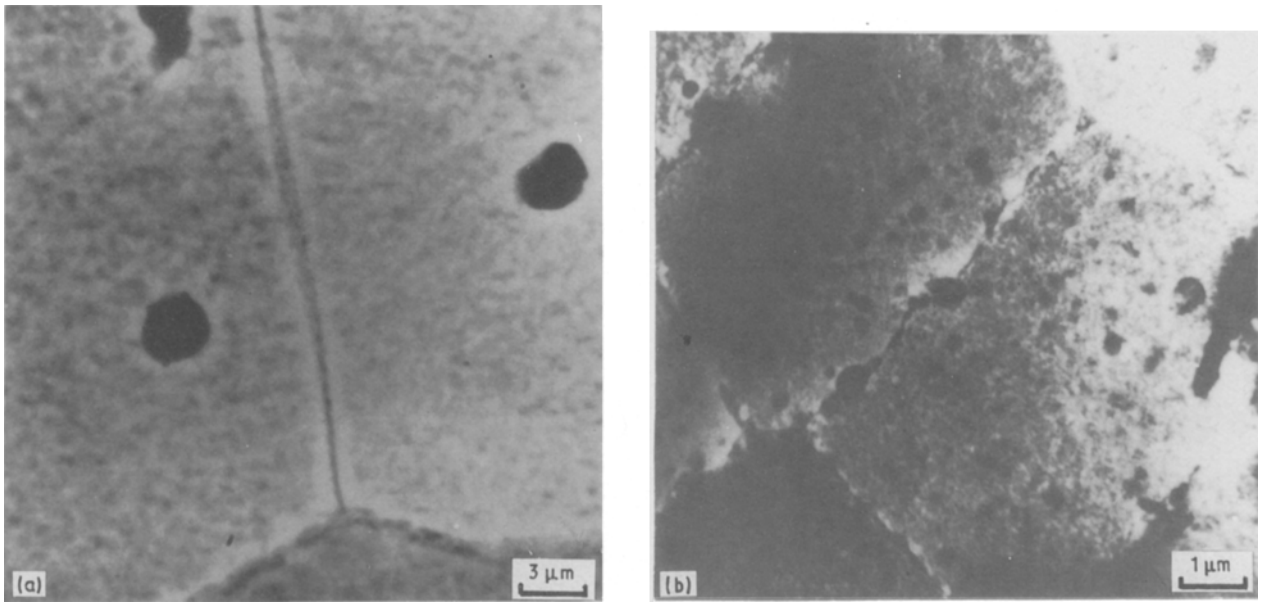

Figure 11 Bright-field transmission electron micrograph narrow PFZ at grain boundary in the RS PM alloys. (a) Alloy 68 (Al–4.93Cu–1.19Li)-T6, (b) Alloy 69 (Al–4.40Cu–1.55Li)-T7.

TABLE I Comparison of the monotonic mechanical properties of the IM Al–4.5Cu–1.2Li alloy with other commercial aluminium alloys

Alloy	Temper	Elastic modulus (GPa)	Yield strength (MPa)	Ultimate strength (MPa)	Elongation (%)
Aluminium[a] (96%)	–	–	30	70	43.0
2020 (Al–4.5Cu–1.2Li)	T651	77	526	567	5.0
2090	T851	79	485	533	10.0
8090	T851	83	578	600	3.85
2024	T851	72	450	485	6.0
7075	T651	71	505	570	11.0

[a] From [58].

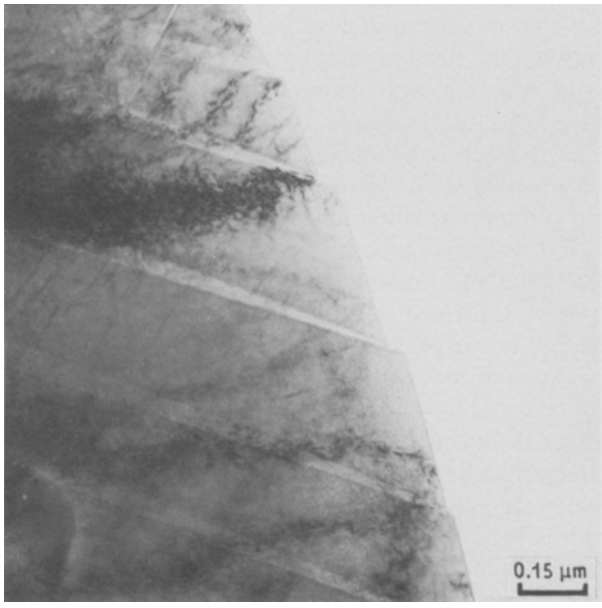

Figure 12 Bright-field transmission electron micrograph showing planar slip bands in the peak-aged tensile samples of the Al–Li–Cu alloy.

tion compared to the I/M counterpart. The improvement is of the order of 10% to 30%. However, the tensile elongation (ductility) and fracture toughness values of the RS PM Al–Cu–Li and the IM Al–Cu–Li alloys are less than those of the conventional IM alloy 7075 in the peak-aged maximum strength condition.

4.3. Fracture surface studies

The monotonic fracture surfaces are helpful in elucidating information on the effect of microstructure on the tensile ductility and fracture properties of the material. For the IM Al–4.5Cu–1.21Li alloy in the peak-aged condition, fracture was normal to the stress axis (Fig. 13a) and predominantly intergranular with traces of transgranular rupture. Secondary cracking was observed parallel to the stress axis along grain boundaries separating transgranular and intergranular fracture regions. A high density of dimples that is observed on the intergranular fracture regions (Fig. 13b) is attributed to the presence of equilibrium phases and particles along grain boundaries. The coarse dimples found on the transgranular fracture

TABLE II Comparison of the room-temperature mechanical properties of the RS PM and IM Al–Cu–Li alloys

Alloy	Temper	Yield strength (MPa)	Ultimate tensile strength (MPa)	Elongation (%)	Reduction in area (%)	K_Q (MN m$^{-3/2}$)
68	T6	565	606	5.8	8.9	9.9–12.1
68	T7	514	556	6.3	15.5	–
69	T6	662	649	4.6	4.0	–
69	T7	623	650	5.3	6.3	11.0–13.2
IM2020	T651	527	567	5.0	–	20.8
IM7075	T651	505	570	11.0	–	27.5–29.7

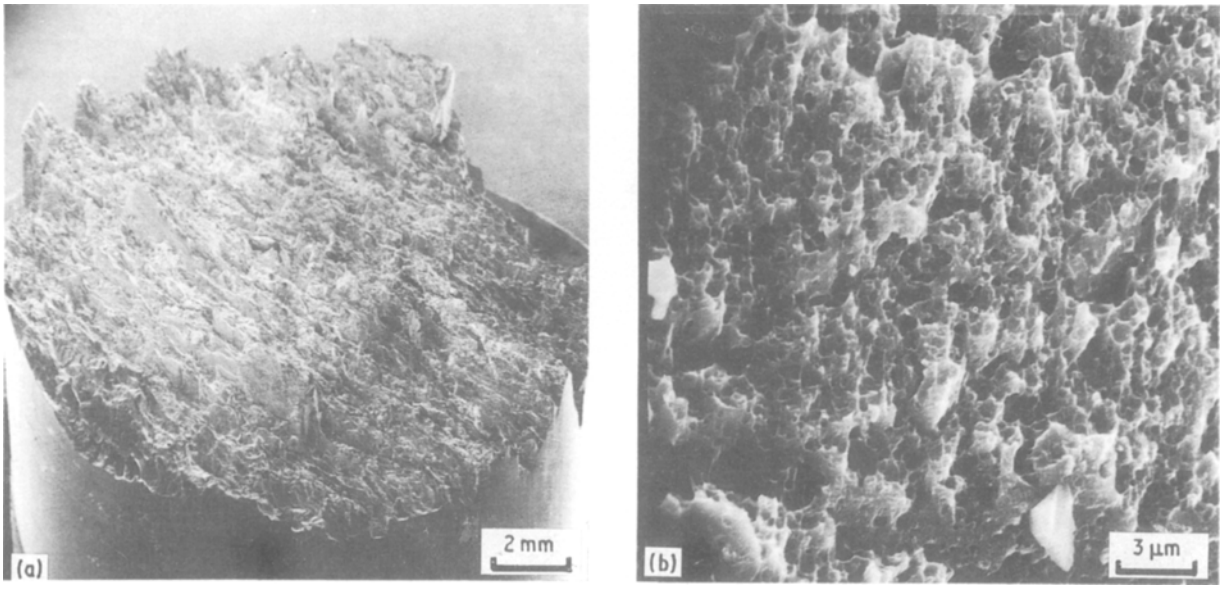

Figure 13 Scanning electron micrographs (a) showing fracture normal to the major stress axis, and (b) of the Al–Li–Cu alloy showing ductile dimples on the intergranular fracture surfaces.

regions are associated with the manganese-containing dispersoid particles, $Al_{20}Cu_2Mn_3$ and Al_6Mn.

In the peak-aged condition the alloy derives much of its strength from the precipitation of fine coherent and partially coherent precipitate particles within the matrix. The ordered precipitates cause the alloy to deform by coarse planar slip (Fig. 12). Also, the presence of fairly large quantities of extremely fine θ′, moderate amounts of T_1 and traces of δ′ matrix-strengthening precipitates ensures that the grains on either side of the common boundary have significant strength. Strain localization and concomitant stress incompatibility at the slip band–grain boundary intersection is accompanied by localized deformation within the soft PFZ which promotes the nucleation of microvoids at grain-boundary precipitates (Fig. 5). The inability of adjacent grains to deform homogeneously contributes to an inability to accommodate strain localization and the resultant stress incompatibility. Therefore, the large difference in strength between the precipitation-strengthened (age-hardened) matrix and the soft PFZ ($\sigma_{matrix} > \sigma_{PFZ}$) promotes intergranular fracture and is detrimental to tensile ductility and toughness.

4.4. Consequences of PFZ on mechanical and fracture behaviour

The effect of PFZs on mechanical properties is of vital interest in alloy design. It is generally realized that the PFZ should influence mechanical properties in some way. Geisler [1] rationalized that in precipitation-hardenable aluminium alloys, the PFZs are softer than the matrix and therefore, a preferred area for plastic flow. Subsequently, Thomas and Nutting proposed that in alloys aged to peak strength, plastic deformation is confined to the PFZs, with no dislocation movement within the matrix [3]. While strain is localized easily in the soft PFZ, the actual influence of the PFZ on the fracture process is not as yet clear. The localized strain in the PFZ should be damaging in that it promotes additional void growth at the grain boundary than would have occurred at a given strain if this were not localized at the grain-boundary PFZ [48, 49].

Ryum [50, 51] and Unwin and Smith [52] actually showed evidence for a small improvement in tensile ductility with increase in width of the grain boundary PFZ. According to Ryum [50] concentration of stress at the intersection of a planar slip band with a grain

boundary might be relaxed by slip in the soft PFZ and consequently, for this mechanism a wider PFZ, would actually be beneficial. The localization of strain in the soft grain-boundary regions promotes the growth of microvoids formed at grain-boundary particles. Coalescence of the microvoids results in dimple-formation type intergranular fracture which is shown schematically in Fig. 14. In the RS PM Al–Cu–Li alloys the presence of incoherent oxide phases can accelerate grain-boundary decohesion. Furthermore, during deformation the soft PFZ would rapidly work harden and eventually fracture. In precipitation-hardenable Al–Cu–Li alloys the strength effect is due primarily to the precipitation of ordered, coherent and partially coherent precipitate phases. Heterogeneous precipitation of equilibrium phases such as δ (AlLi) is not an easy process considering:

(a) the large α/δ misfit,
(b) the concomitant change in lithium concentration, and
(c) the new crystal structure (an NaTl-type bcc structure).

The decomposition of the supersaturated Al–Li–Cu solid solution can be summarized as follows

$$\text{Supersaturated solid solution} \begin{cases} \nearrow \text{GP zones} \rightarrow \theta'' \rightarrow \theta'(Al_2Cu) \rightarrow \theta \\ \searrow \delta'(Al_3Li) \rightarrow \delta(AlLi) \end{cases}$$

The micromechanisms governing the deformation and fracture characteristics of these alloys depend on the intrinsic microstructural features such as: (i) the coherency and distribution of matrix strengthening precipitates, (ii) particle size and distribution, (iii) nature of grain-boundary precipitates, (iv) particle volume fraction, and (v) degree of ordering. Consideration of the strengthening mechanism in peak-aged alloys is important because it markedly affects the deformation process. During deformation, the ordered coherent and partially coherent precipitates [$\delta'(Al_3Li)$, $\theta'(Al_2Cu)$ and T_1 (Al_2CuLi)] in the alloy are easily sheared by the motion of dislocations on close packed planes {1 1 1} and in the close-packed directions. The strength of the alloy is progressively reduced when the precipitates are sheared by dislocations. This is because the effective cross-section of the particles decreases as they are sheared by dislocations.

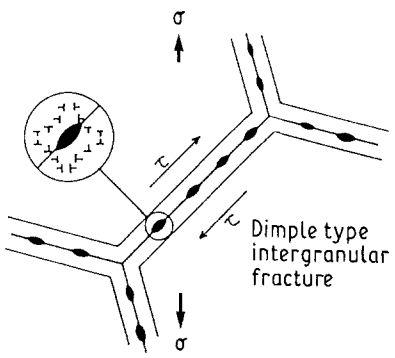

Figure 14 Schematic representation of the dimple formation-type intergranular fracture process.

The destruction of strengthening precipitates by shearing results in a local decrease in resistance to dislocation motion and a concentration of slip in narrow bands through the grain. The slip concentration causes localization of strain at the grain boundary. The extent of strain localization depends on the difference in flow stress between the two adjacent regions. Consequently, the effects of strain localization become pronounced in alloys aged to peak strength. This observation is consistent with the reported lower tensile elongation (ductility) values of the peak-aged (T6) RS PM Al–Cu–Li alloys (Alloy 68 and Alloy 69), when compared to those for the T7 temper for the same alloys.

Localization of strain causes high local stresses to build up at regions where the slip band impinges on the grain boundary. Mott [53] suggested that the stress concentration around the piled-up dislocations at the end of the slip band may be adequate to initiate a crack. Stroh [54] formulated this concept mathematically. According to Stroh the stress concentration factor of a pile-up increases with the square root of the length of the pile-up. The number of dislocations that are associated with the pile-up can be about 100 to 1000. The tensile stress, say σ, ahead of a blocked slip band is maximum at about 70° to the slip plane and the maximum stress is expressed as

$$\sigma_{max} = 2\sigma_0\left(\frac{D_p}{3r}\right)^{1/2}$$

where σ_0 is the externally applied stress, n is the number of dislocations in the slip band, D_p is the pile-up length and $2r$ is the length of the crack.

In the presence of precipitate-free zones, plastic relaxation occurs within the soft zones. The extent of plastic relaxation is dependent on the width of the PFZ (Fig. 15). The narrow slip bands are held up at the boundary of the PFZ. The long-range stresses caused by the pile-up of dislocations on the blocked slip band produce tensile stresses that equal and exceed the critical fracture strength across the grain boundaries. Owing to the presence of grain-boundary particles, the boundaries represent weakened surfaces [55–57]. As a result, conditions for low-energy grain boundary or intergranular fracture are favoured.

The PFZs adjacent to the grain boundary in the IM Al–1.21Li–4.5Cu alloy are lithium depleted and considerably weaker than the matrix ($\sigma_{PFZ} < \sigma_{matrix}$). Consequently, they are potential sites for preferential plastic deformation resulting in high local stress concentrations at grain-boundary triple junctions (Fig. 16a). During deformation the cracks nucleate at either the grain-boundary triple junctions or at grain-boundary particles and propagate intergranularly within the soft PFZs (Fig. 16b). A wide PFZ could cause a loss in strength with a concomitant increase in ductility.

The tensile fracture behaviour of the RS PM alloys were found to be predominantly intercrystalline. Local cracking was observed in areas of high concentration of oxide particles. The presence of PFZs only promoted such premature cracking. The facet-type

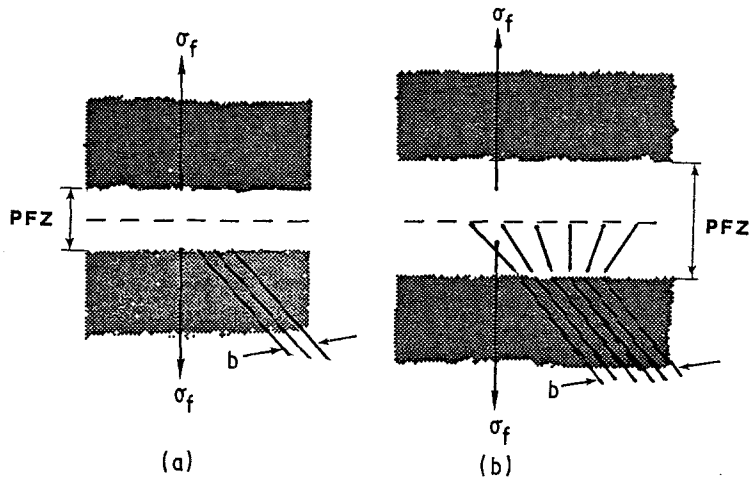

Figure 15 Schematic drawing showing the extent of plastic relaxation within the PFZ: (a) when aged at a low temperature, (b) when aged at a higher temperature. b is the width of planar slip band.

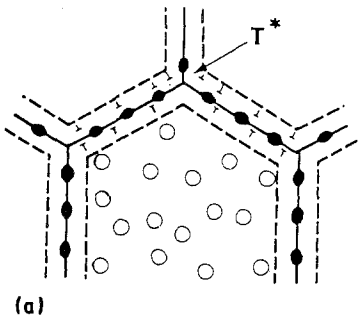

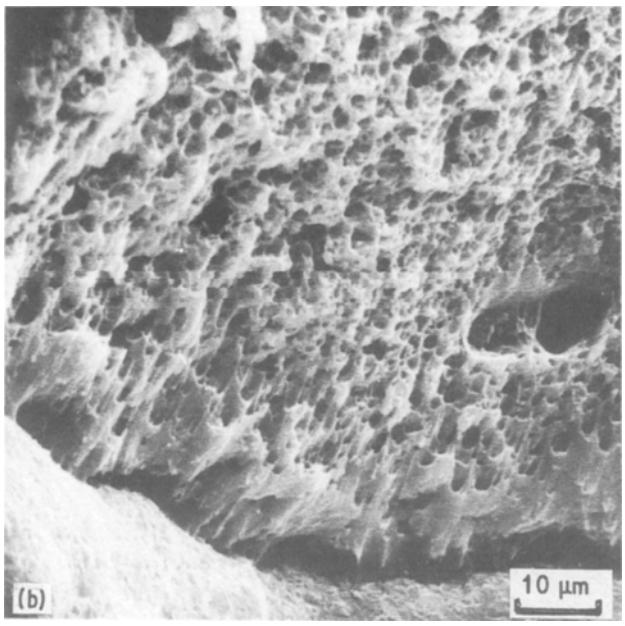

Figue 16 (a) Schematic drawing showing PFZ at grain boundary and build-up of high local stress concentration at the grain-boundary triple junction. (b) Scanning electron micrograph showing low-energy intergranular fracture in the peak-aged Al–Cu–Li alloy following crack initiation at the grain boundary.

features observed on the grain boundary were associated with poorly bonded powder boundaries [30]. The detrimental effect of oxide stringers on fracture behaviour was found to be almost as important as the nature and distribution of second-phase particles in the alloy. The rapidly solidified alloys also revealed intercrystalline cracking after small amounts of cold stretching. This was largely attributed to the presence of oxide stringers and narrow PFZs.

5. Conclusions

The general conclusions of the present study of the presence and consequences of PFZs in an ingot metallurgy Al–4.5Cu–1.21Li alloy are summarized as follows.

1. In this precipitation-hardenable alloy narrow PFZs were found along the high-angle grain boundaries and at grain-boundary triple junctions.

2. Microstructure of the ingot metallurgy Al–4.5Cu–1.21Li alloy is partially recrystallized with the large recrystallized grains elongated parallel to the rolling direction and comprising of (i) the coarse constituent particles of the larger type (1 to 10 μm in the longest dimension), and (ii) of the smaller type (0.2 to 1 μm).

3. Strengthening precipitates in the alloy in the peak-aged condition are fine, small in size, closely spaced and coherent or partially coherent with the matrix.

4. While the strength of the alloy was comparable, the tensile ductility (elongation to failure) was inferior to existing high-strength commercial aluminium alloys 7075-T651, 2090-T851, 8090-T851 and 2024-T851.

5. The strength and ductility of the IM alloy were inferior to those of the rapidly solidified PM alloys of near equivalent composition.

6. The deformation was inhomogeneous "planar-slip" with a tendency towards strain localization.

7. Fracture of the IM alloy was predominantly low-energy intergranular rupture and is rationalized in terms of: (i) strain localization and stress incompatibility effects at the grain boundary, and (ii) to differences in strength between the precipitation strengthened matrix and the soft PFZ.

8. The role of the PFZs as potential sites for preferential plastic deformation and their detrimental influence on strength, ductility and fracture resistance, is critically examined.

Acknowledgements

Dr T. S. Srivatsan thanks the US Navy, Naval Surface Weapons Center and the Ohio Board of Regents (Grant No. OBR 5-34021) for providing partial support during this study. Dr E. J. Lavernia acknow-

ledges the financial support of University Technology Transfer Inc., and the Army Research Office.

References

1. A. H. GEISLER, *Trans. AIME* **180** (1949) 230.
2. *Idem*, "Phase Transformation in Solids" (Wiley, New York, 1951) p. 387.
3. G. THOMAS and J. NUTTING, *J. Inst. Metals* **88** (1959–60) 81.
4. J. L. TAYLOR, *ibid.* **92** (1963–64) 301.
5. J. D. EMBURY and R. B. NICHOLSON, *Acta Metall.* **13** (1965) 403.
6. A. KELLY and R. B. NICHOLSON, "Progress in Materials Science", Vol. 10, edited by Bruce Chalmers. (Pergamon Press, New York, 1963).
7. G. W. LORIMER and R. B. NICHOLSON, "The Mechanisms of Phase Transformation in Crystalline Solids" (The Institute of Metals, London, 1969) p. 36.
8. *Idem*, *Acta Metall.* **14** (1966) 1009.
9. P. N. T. UNWIN, G. W. LORIMER and R. B. NICHOLSON, *ibid.* **17** (1969) 1363.
10. W. F. SMITH and N. J. GRANT, *Trans. ASM* **92** (1969) 44.
11. T. H. SANDERS Jr, Final Report for the Naval Air Development Center, NADC Contract no. N62269-76-0271, June 1979.
12. A. J. CORNISH and M. K. B. DAY, *J. Inst. Metals* **97** (1969) 44.
13. P. N. T. UNWIN and R. B. NICHOLSON, *Acta Metall.* **17** (1969) 1379.
14. N. RYUM, *ibid.* **17** (1969) 921.
15. A. K. VASUDEVAN and R. D. DOHERTY, *ibid.* **35** (1987) 1193.
16. E. A. STARKE Jr, *J. Metals* **54** (1970) pp. 1–10.
17. D. W. PASHLEY, M. H. JACOBS and J. T. VIETZ, *Philos. Mag.* **16** (1967) 51.
18. R. B. NICHOLSON, *J. Inst. Metals* **95** (1967) 91.
19. P. E. DOHERTY and R. S. DAVIS, *Acta Metall.* **7** (1959) 118.
20. G. A. CHADWICK, *Philos. Mag.* **14** (1966) 1295.
21. P. N. T. UNWIN, G. W. LORIMER and R. B. NICHOLSON, *Acta Metall.* **17** (1969) 1363.
22. J. M. SILCOCK, *J. Inst. Metals* **88** (1959–60) 357.
23. B. NOBLE and G. E. THOMPSON, *Met. Sci. J.* **5** (1971) 114.
24. D. B. WILLIAMS and J. W. EDINGTON, *ibid.* **9** (1975) 529.
25. B. P. GU, J. H. KULWICKI, G. L. LIEDL and T. H. SANDERS Jr, *Mater. Sci. Engng* **70** (1985) 217.
26. S. C. JHA, T. H. SANDERS Jr and M. A. DAYANANDA, *Acta Metall.* **35** (1987) 473.
27. T. H. SANDERS Jr, E. A. LUDWICZAK and R. R. SAWTELL, *Mater. Sci. Engng* **43** (1980) 247.
28. O. JENSRUD and N. RYUM, *ibid.* **64** (1984) 229.
29. S. KANG and N. J. GRANT, in "Aluminium–Lithium Alloys II", edited by T. H. Sanders Jr and E. A. Starke Jr (The Metallurgical Society of AIME, Warrendale, Pennsylvania, 1985) pp. 469–483.
30. S. KANG and N. J. GRANT, *Metall. Trans.* **18A** (1987) 2037.
31. A. GYSLER, R. E. CROOKS and E. A. STARKE Jr, in "Aluminium–Lithium Alloys", edited by T. H. Sanders Jr and E. A. Starke Jr (Metallurgical Society of AIME, Warrendale, Pennsylvania, 1981) p. 263.
32. E. J. COYNE Jr, T. H. SANDERS Jr and E. A. STARKE Jr, *ibid.*, p. 293.
33. J. G. RINKER, M. MAREK and T. H. SANDERS Jr, *Mater. Sci. Engng* **64** (1984) 203.
34. T. S. SRIVATSAN, Doctor of Philosophy Thesis, Georgia Institute of Technology (1984).
35. E. A. STARKE Jr and F. S. LIN, *Metall. Trans.* **13A** (1982) 2259.
36. J. M. SILCOCK, T. J. HEAL and H. K. HARDY, *J. Inst. Metals* **84** (1955–56) 23.
37. J. D. BOYD and R. B. NICHOLSON, *Acta Metall.* **19** (1971) 1379.
38. J. P. LYLE and W. S. CEBULAK, *Metall. Trans.* **6A** (1975) 685.
39. J. R. PICKENS, *J. Mater. Sci.* **16** (1981) 1437.
40. M. J. COOPER, M. NAUER, R. BAUMAN, R. F. SINGER, in Proceedings of the 1987 Conference on "Powder Metallurgy Aerospace Materials", Lucerne, Switzerland, November 1987.
41. R. LALAUZE, I. GUILLEMIN and C. PIJOLAT, *J. Thermal Analy.* **31** (1986) 1109.
42. S. FOX, H. M. FLOWER and D. S. McDARMAID, in "Aluminium-Lithium III", Proceedings of the Third International Conference, edited by C. Baker, S. J. Harris, P. J. Gregson and C. J. Peel (The Institute of Metals, London, 1986) p. 263.
43. M. AHMAD, *Metall. Trans.* **18A** (1987) 681.
44. F. R. BILLMAN, J. C. KULI Jr, G. J. HILDEMAN, J. E. PETIT and J. A. WALKER, "Proceedings of the Third International Conference on Rapid Solidification", (National Bureau of Standards, Gaithersburg, Maryland, 1982) p. 532.
45. W. L. OTTO Jr, "Metallurgical Factors Controlling Structure in High Strength Aluminum Products", Air Force Materials Laboratory, AFML-TR-76-60, May 1976.
46. E. J. LAVERNIA and N. J. GRANT, *Mater. Sci. Engng* **98** (1988) 381.
47. Y. W. KIM, "Progress in Powder Metallurgy", Vol. 54, Proceedings of the 1987 Powder Metallurgy Exhibition (Metal Powder Industries Federation and the American Powder Metallurgy Institute, Princeton, New Jersey, 1987) p. 13.
48. E. HORNBOGEN and M. GRAF, *Acta Metall.* **25** (1977) 877.
49. J. D. EMBURY and E. NESS, *Z. Metallkde.* **65** (1974) 45.
50. N. RYUM, *Acta Metall.* **16** (1968) 327.
51. *Idem*, *ibid.* **17** (1969) 921.
52. P. T. UNWIN and G. C. SMITH, *J. Inst. Metals* **97** (1969) 300.
53. N. F. MOTT, *Proc. R. Soc.* **200A** (1953) 1.
54. A. H. STROH, *ibid.* **223A** (1954) 404.
55. *Idem*, *ibid.* **232A** (1955) 550.
56. A. K. VASUDEVAN, E. A. LUDWICZAK, S. F. BAUMANN and R. D. DOHERTY, *Mater. Sci. Engng* **72** (1985) L25.
57. R. BECKER, A. NEEDLEMAN, S. SURESH, V. TVERGAARD and A. K. VASUDEVAN, *Acta Metall.* **37** (1989) 99.
58. J. E. HATCH, "Aluminium".

Received 14 August 1989
and accepted 1 February 1990